Molecular-orbital representation with random U(1) variables

Tomonari Mizoguchi [*] and Yasuhiro Hatsugai

Department of Physics, University of Tsukuba, Tsukuba, Ibaraki 305-8571, Japan

We propose random tight-binding models that host macroscopically degenerate zero-energy modes and belong to the unitary class. Specifically, we employ the molecular-orbital representation, where a Hamiltonian is constructed by a set of nonorthogonal orbitals composed of linear combinations of atomic orbitals. By setting the coefficients appearing in molecular orbitals to be random U(1) variables, we can make the models belong to the unitary class. We find two characteristic behaviors that are distinct from the random real-valued molecular-orbital model. Firstly, a finite-energy gap opens on top of the degenerate zero-energy modes. Secondly, besides the zero-energy modes, we also argue that the band center of the finite-energy modes is critical, which is inherited from the dual counterpart, namely, the random-phase model on a bipartite lattice. Furthermore, as a by-product of this model-construction scheme, we also construct the random tight-binding model on a composite lattice, where we also find a realization of critical states.

I. INTRODUCTION

The effects of disorders on electronic systems have been a central issue in condensed matter physics. Metal-insulator transition induced by disorders, i.e., the Anderson localization, is one of the most striking phenomena caused by disorders [1,2], and there have been tremendous amounts of research activities since its proposal. More recently, the effects of disorders on systems with exotic electronic structures have been studied extensively. For instance, Dirac fermions, characterized by vanishing density of states at the Dirac points, exhibit rich physics in the presence of disorders [3–8]. Another example of exotic electronic structures is flat bands, i.e., the completely dispersionless bands in the entire Brillouin zone. In flat-band systems, macroscopic degeneracy of the single-particle spectrum allows us to construct localized eigenstates even without disorders [9–11]. Then, they are expected to be highly sensitive to disorders. Indeed, various characteristic phenomena due to the interplay between flat bands and disorders have been reported [12–19].

Besides the electronic structures, the symmetry and dimensionality also play a crucial role in determining the nature of the Anderson localization [20]. In theoretical analysis of tight-binding models, the type of disorders (e.g., random potentials, random hoppings, random flux, etc.) and the lattice structures are two key ingredients for determination of the symmetry class. In this respect, the previous works on disordered flat-band systems mainly focus on the case where random on-site potentials are introduced to a flat-band model, and a Hamiltonian matrix is consequently a real matrix [12–14,19]. In contrast to those works, we have developed yet another direction of studying random flat-band models, that is, tailoring the models such that macroscopic degeneracy can be exactly

retained even in the presence of disorders. To be more specific, we have studied tight-binding Hamiltonians that are written down by a set of nonorthogonal and unnormalized orbitals constructed by a linear combination of atomic orbitals (AOs) and whose total number is smaller than that of the AOs [21]. We name such construction the "molecular-orbital" (MO) representation [22–29]. Along this line, in the previous works, we consider the MO models where the coefficients appearing in MOs are random real values [30]. We refer to this type of models as the real-valued random MO models henceforth. We have found that the probability density of zero-energy modes is seemingly characteristic and resembles that of the critical state, but its scaling behavior upon changing the system size obeys that of the extended state [27,29].

With this as the background, in this paper, we consider the random MO models with different type of randomness from that in the previous works. Specifically, we construct the MOs such that the coefficients are random U(1) variables, which breaks the time-reversal symmetry and thus the universality class becomes unitary. We refer to the models constructed in this way as the random-phase MO models.

We first study the checkerboard model to illustrate the idea of model construction. A key feature is that this model is a dual of the random-phase (also referred to as the random vector potential or the random flux) square lattice model, which has been studied intensively as a prime example of the random lattice fermion models in the unitary class [31–40].

By the numerical calculations, we elucidate the similarities and differences between the random-phase MO models and the real-valued random MO models. On the energy spectrum, a finite-energy gap opens on top of the degenerate zero-energy modes, which is in contrast to the real-valued random MO model. Meanwhile, the probability density distribution of the zero-energy modes has similar behavior to that of the real-valued random MO model in that its finite-size scaling behavior of the inverse participation ratio (IPR) obeys

*mizoguchi@rhodia.ph.tsukuba.ac.jp

that of extended states. Besides the zero-energy modes, we also find a characteristic feature in the finite-energy modes, namely, the band center of the finite-energy modes is a critical state, which is inherited from the random-phase square lattice model. Notably, the random-phase MO model itself is not chiral symmetric, although the chiral symmetry plays an important role in the emergence of the critical state in the random-phase square-lattice model.

We additionally show that the random-phase MOs used to describe the checkerboard model can be used to construct a model defined on a composite lattice of the square and checkerboard lattices, i.e., the Lieb lattice. In fact, the authors have applied a similar model construction scheme to a kind of topological insulators, called the square-root topological insulators [41,42]. We show that, in the Lieb lattice model, the critical states inherited from the square-lattice random-phase model appear at the center of the positive- and negative-energy sectors in a pairwise manner.

Subsequently to the checkerboard and Lieb-lattice models, we also apply this construction method to the kagome model, where we find that the results are qualitatively the same as those of the checkerboard model. In addition, we also argue the composite-lattice model of this series; the corresponding composite-lattice model is a decorated honeycomb lattice model, where we again find the qualitatively same results as those of the Lieb-lattice model. These results indicate the ubiquity of the present model construction by the random-phase MO representation.

The rest of this paper is organized as follows. In Sec. II, we introduce the random-phase MO model on a checkerboard lattice, and elucidate its basic properties, including the dual relation to the random-phase square-lattice model. Then, in Sec. III, we present our numerical results on the spectrum and wave functions. We focus on two aspects, namely, the gap opening between the degenerate zero-energy modes and the lowest finite-energy modes, and the critical nature of the center of the finite-energy modes. In Sec. IV, we argue that the random-phase MO introduced to describe the checkerboard model can be used to construct the composite-lattice model, namely, the Lieb-lattice model. In Sec. V, we apply the same construction to the kagome lattice, and we show the parallel numerical results to the checkerboard model. The results for the composite lattice, namely, the decorated honeycomb model, are also shown. The summary of this paper is presented in Sec. VI.

II. MODEL CONSTRUCTION SCHEME: CHECKERBOARD LATTICE

In this section, we introduce a random-phase MO model on a checkerboard lattice [Fig. 1(a)]. The system consists of $L \times L (= N_{\text{u.c.}})$ unit cells and the periodic boundary condition is imposed. At each site i of the checkerboard lattice, we define the AO whose annihilation operator is written as c_i. The site i is specified by the unit-cell position $\boldsymbol{R} = R_1 \boldsymbol{a}_1 + R_2 \boldsymbol{a}_2$ and the sublattice index A/B.

On this lattice, we consider a tight-binding Hamiltonian:

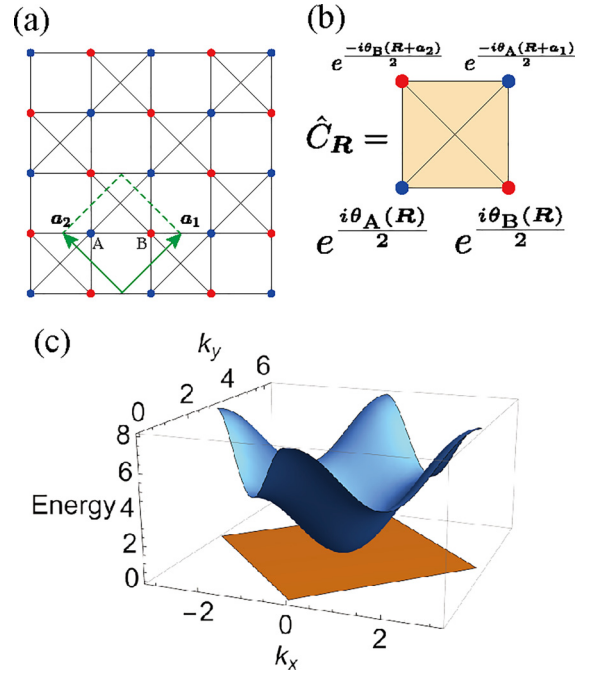$$H = \sum_{\boldsymbol{R}} \hat{C}_{\boldsymbol{R}}^{\dagger} \hat{C}_{\boldsymbol{R}}, \tag{1}$$

FIG. 1. (a) Checkerboard lattice. Two lattice vectors are $\boldsymbol{a}_1 = (1, 1)$ and $\boldsymbol{a}_2 = (-1, 1)$. (b) Schematic figure of $\hat{C}_{\boldsymbol{R}}$. (c) The dispersion relation for the clean limit [i.e., $\theta_{\text{A/B}}(\boldsymbol{R}) = 0$].

where

$$\hat{C}_{\boldsymbol{R}} = e^{i\theta_{\text{A}}(\boldsymbol{R})/2} c_{\boldsymbol{R},\text{A}} + e^{i\theta_{\text{B}}(\boldsymbol{R})/2} c_{\boldsymbol{R},\text{B}}$$
$$+ e^{-i\theta_{\text{A}}(\boldsymbol{R}+\boldsymbol{a}_1)/2} c_{\boldsymbol{R}+\boldsymbol{a}_1,\text{A}} + e^{-i/\theta_{\text{B}}(\boldsymbol{R}+\boldsymbol{a}_2)/2} c_{\boldsymbol{R}+\boldsymbol{a}_2,\text{B}}. \tag{2}$$

See Fig. 1(b) for the schematic figure of $\hat{C}_{\boldsymbol{R}}$. It is worth noting that the MOs are defined on lattice sites of a square lattice which are placed at the center of the crossed squares of a checkerboard lattice. In Eq. (2), the phase $\theta_{\text{A/B}}(\boldsymbol{R}) \in [-\pi, \pi]$ is a random variable obeying the uniform distribution. The choice of MOs in Eq. (2) might look fine-tuned because the phase factors appearing in neighboring MOs are not independent. For instance, the variable $\theta_{\text{A}}(\boldsymbol{R})$ appears both in $\hat{C}_{\boldsymbol{R}}$ and in $\hat{C}_{\boldsymbol{R}-\boldsymbol{a}_1}$. In Appendix A, we elucidate the relation between this model and the model where all phase factors are random
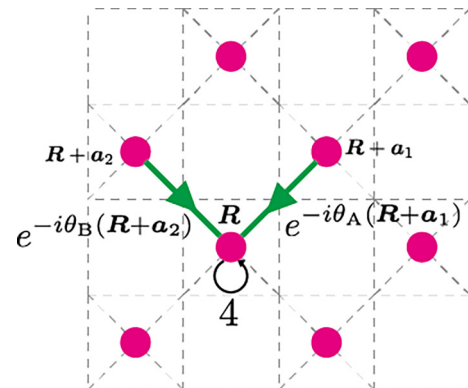

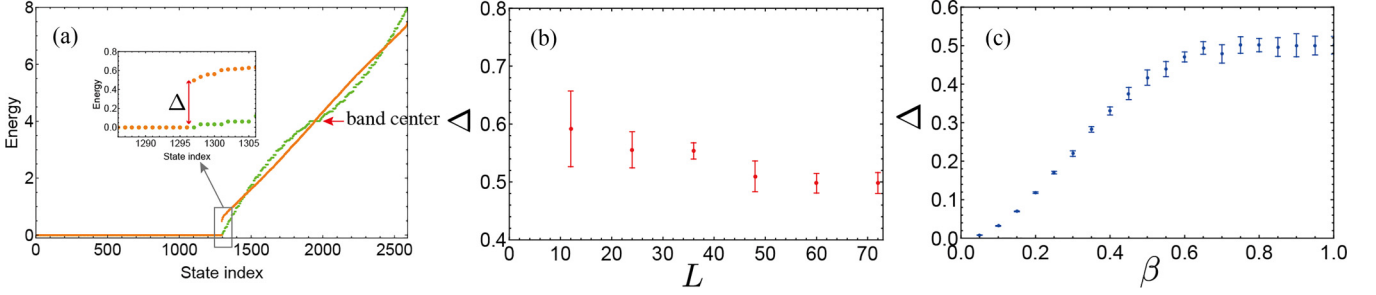FIG. 2. Schematic figure of the square-lattice tight-binding model with random-phase factor, corresponding to Υ.

FIG. 3. (a) Energy spectrum for the system with $L = 36$. Orange (green) dots correspond to the random (clean) system. (b) The gap Δ as a function of L. (c) The gap as a function of β for $L = 60$. For (b) and (c), the average and the standard deviation are calculated for ten independent configurations of θ's.

variables. We call $\hat{C}_{\boldsymbol{R}}$ the MO since it consists of a local linear combination of AOs.

We align all the AOs in a column vector form, which we write as $\hat{\boldsymbol{c}}$; similarly, we align the MO in a column vector form, which we write as $\hat{\boldsymbol{C}}$. Using these, we can rewrite the Hamiltonian of Eq. (1) as

$$H = \hat{\boldsymbol{c}}^\dagger \mathcal{H} \hat{\boldsymbol{c}}, \quad \mathcal{H} = \Psi \Psi^\dagger, \tag{3}$$

where Ψ is a $2N_{\text{u.c.}} \times N_{\text{u.c.}}$ matrix defined such that it satisfies $\hat{\boldsymbol{C}}^\dagger = \hat{\boldsymbol{c}}^\dagger \Psi$. Then, the single-particle eigenenergies and eigenstates are obtained by solving the eigenvalue equation of the matrix $\mathcal{H}$.

In fact, Eq. (3) indicates that there are at least $N_{\text{u.c.}}$ zero-energy eigenstates of $\mathcal{H}$. To be specific, as $\Psi^\dagger$ is the nonsquare matrix where the number of rows is lesser than that of columns, the dimension of the kernel of the linear map expressed by $\Psi^\dagger$ is equal to or greater than $N_{\text{u.c.}}$. In other words, there exist vectors $\boldsymbol{\phi}_\ell^{\text{ZM}}$ ($\ell = 1, \ldots, N_{\text{u.c.}}$) such that $\boldsymbol{\phi}_\ell^{\text{ZM}}$ satisfies $\Psi^\dagger \boldsymbol{\phi}_\ell^{\text{ZM}} = 0$. Then, such vectors also satisfy $\mathcal{H} \boldsymbol{\phi}_\ell^{\text{ZM}} = \Psi(\Psi^\dagger \boldsymbol{\phi}_\ell^{\text{ZM}}) = 0$. In the following, we assume that $\boldsymbol{\phi}_\ell^{\text{ZM}}$ is normalized, namely, $(\boldsymbol{\phi}_\ell^{\text{ZM}})^\dagger \boldsymbol{\phi}_\ell^{\text{ZM}} = 1$ holds.

A. Review of clean-limit properties

Without phase factors, i.e., $\theta_{\text{A}}(\boldsymbol{R}) = \theta_{\text{B}}(\boldsymbol{R}) = 0$, the model is the conventional checkerboard lattice model with the nearest-neighbor hoppings being 1 and the on-site potential being 2. In this case, the eigenenergy of the dispersive band as a function of a crystal momentum is easily obtained as $E_{\boldsymbol{k}} = 4 + 2(\cos \boldsymbol{k} \cdot \boldsymbol{a}_1 + \cos \boldsymbol{k} \cdot \boldsymbol{a}_2)$; the other band is the flat band with the eigenenergy being 0. The band structure is

depicted in Fig. 1(c), where we see the quadratic band touching at $\boldsymbol{k} = \frac{\boldsymbol{b}_1 + \boldsymbol{b}_2}{2} = (0, \pi)$ [$\boldsymbol{b}_1 = (\pi, \pi)$ and $\boldsymbol{b}_2 = (-\pi, \pi)$ are the reciprocal lattice vectors]. Recently, several theoretical understandings of this type of band touching were proposed [10,18,43–46]. From the viewpoint of the MO representation, the origin of the quadratic band touching is the linear dependence of the MOs. To be specific, in the clean limit, the following relation holds:

$$\sum_{\boldsymbol{R}} (-1)^{R_1 + R_2} \hat{C}_{\boldsymbol{R}} = 0. \tag{4}$$

This means that the number of linearly independent MOs (or the rank of $\Psi^\dagger$) is $N_{\text{u.c.}} - 1$, rather than $N_{\text{u.c.}}$. Recalling the fact that the zero modes belong to the kernel of $\Psi^\dagger$, the degeneracy of zero modes is $N_{\text{u.c.}} + 1$, which leads to band touching of the bottom of the dispersive band to the flat band.

B. Semipositivity of $\mathcal{H}$

We now turn to the disordered case. Firstly, it is important to point out that, from Eq. (3), $\mathcal{H}$ is positive semidefinite for generic random phases. A straightforward proof of this is as follows: let $\boldsymbol{\phi}$ be an arbitrary $2N_{\text{u.c.}}$-component column vector. Then, we have $\boldsymbol{\phi}^\dagger \mathcal{H} \boldsymbol{\phi} = |\Psi^\dagger \boldsymbol{\phi}|^2 \geqslant 0$, which indicates the semipositivity of $\mathcal{H}$. This is enough, but here we present an alternative proof, which gives a useful insight on Ψ and $\Psi^\dagger$ (see Sec. II C for details). We introduce a Hermitian matrix

$$\bar{\mathcal{H}} = \begin{pmatrix} \mathcal{O}_{N_{\text{u.c.}}, N_{\text{u.c.}}} & \Psi^\dagger \\ \Psi & \mathcal{O}_{2N_{\text{u.c.}}, 2N_{\text{u.c.}}} \end{pmatrix}, \tag{5}$$
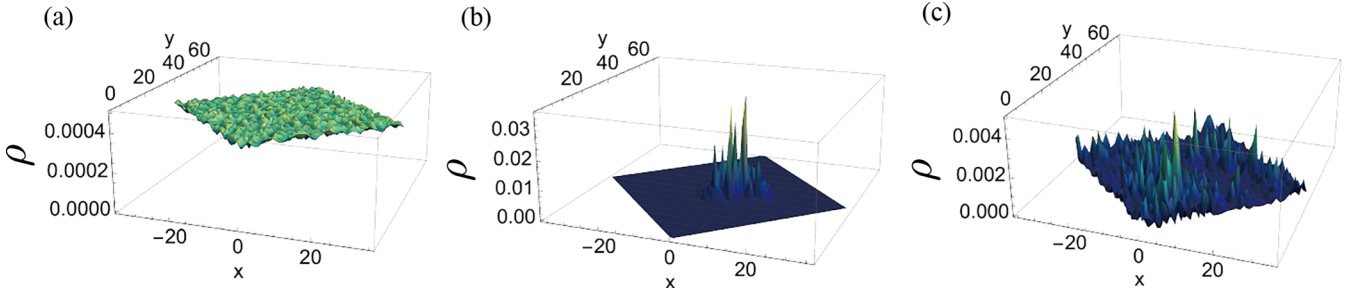

FIG. 4. The probability density for (a) the zero modes, (b) the lowest finite-energy mode, and (c) the center of the finite-energy modes. We set $L = 36$.
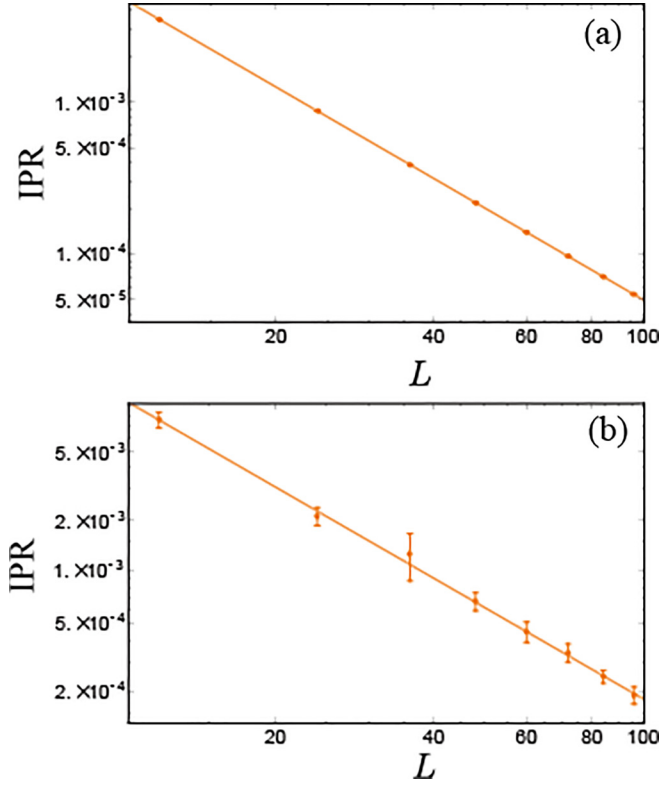
FIG. 5. IPR for (a) the degenerate zero modes and (b) the center of the finite-energy modes. The line represents the fitting function, IPR=AL^{-B}, with (a) A=0.50, B = 1.99 and (b) A = 0.60, B=1.76. The average and the standard deviation are calculated for ten independent configurations of θ's.

where $\mathcal{O}_{n,m}$ denotes a $n \times m$ zero matrix. Then, the square of the matrix $\bar{\mathcal{H}}$ is block-diagonalized as

$$\bar{\mathcal{H}}^2 = \begin{pmatrix} \Upsilon & \mathcal{O}_{N_{\text{u.c.}},2N_{\text{u.c.}}} \\ \mathcal{O}_{2N_{\text{u.c.}},N_{\text{u.c.}}} & \mathcal{H} \end{pmatrix}, \qquad (6)$$

where $\Upsilon = \Psi^{\dagger}\Psi$. The matrix $\bar{\mathcal{H}}^2$ is obviously positive semidefinite, and so are Υ and $\mathcal{H}$, since they are top-left and bottom-right blocks of $\bar{\mathcal{H}}^2$, respectively.

C. Relation to the square-lattice model and its implication

In the following discussions, Υ of Eq. (6) plays a crucial role in understanding the properties of $\mathcal{H}$. In fact, the eigenvalues of Υ are in common with those of $\mathcal{H}$. This is simply understood by the following relation [47–49]:

$$\mathcal{H}\Psi = \Psi\Upsilon. \qquad (7)$$

Using this relation, we find the following: Let $\boldsymbol{u}_{\ell}$ be a normalized eigenvector of Υ with the eigenvalue ε_{ℓ}. Then, we have

$$\mathcal{H}(\Psi\boldsymbol{u}_{\ell}) = \Psi(\Upsilon\boldsymbol{u}_{\ell}) = \varepsilon_{\ell}(\Psi\boldsymbol{u}_{\ell}), \qquad (8)$$

meaning that $\Psi\boldsymbol{u}_{\ell}$ is an eigenvector of $\mathcal{H}$ with the eigenvalue ε_{ℓ}, up to the normalization constant. Further, noting that $|\Psi\boldsymbol{u}_{\ell}|^2 = \boldsymbol{u}_{\ell}^{\dagger}\Psi^{\dagger}\Psi\boldsymbol{u}_{\ell} = \boldsymbol{u}_{\ell}^{\dagger}\Upsilon\boldsymbol{u}_{\ell} = \varepsilon_{\ell}$, we find that the normalized eigenvector of $\mathcal{H}$ with the eigenenergy ε_{ℓ} is

$$\boldsymbol{\phi}_{\ell}^{\text{NZM}} = \frac{1}{\sqrt{\varepsilon_{\ell}}}\Psi\boldsymbol{u}_{\ell}. \qquad (9)$$

Importantly, in the present model, Υ is given as

$$\Upsilon = 4\hat{I}_{N_{\text{u.c.}}} + \tilde{\mathcal{H}}^{\text{sq}}, \qquad (10)$$

where $\hat{I}_n$ represents the $n \times n$ identity matrix and $\tilde{\mathcal{H}}^{\text{sq}}$ corresponds to the square-lattice tight-binding model with the random-phase factor (Fig. 2):

$$[\tilde{\mathcal{H}}^{\text{sq}}]_{\boldsymbol{R},\boldsymbol{R}'} = \begin{cases} e^{-i\theta_{\text{A}}(\boldsymbol{R}+\boldsymbol{a}_1)}, & \boldsymbol{R}' = \boldsymbol{R} + \boldsymbol{a}_1 \\ e^{i\theta_{\text{A}}(\boldsymbol{R})}, & \boldsymbol{R}' = \boldsymbol{R} - \boldsymbol{a}_1 \\ e^{-i\theta_{\text{B}}(\boldsymbol{R}+\boldsymbol{a}_2)}, & \boldsymbol{R}' = \boldsymbol{R} + \boldsymbol{a}_2 \\ e^{i\theta_{\text{B}}(\boldsymbol{R})}, & \boldsymbol{R}' = \boldsymbol{R} - \boldsymbol{a}_2 \\ 0, & \text{otherwise.} \end{cases} \qquad (11)$$

This model of the square-lattice random-phase (or the random-flux) model, has been intensively studied in the literature [31–40]. Note that $\tilde{\mathcal{H}}^{\text{sq}}$ is chiral symmetric, that is, $\tilde{\mathcal{H}}^{\text{sq}}$ satisfies $\{\tilde{\mathcal{H}}^{\text{sq}}, \Gamma\} = 0$ with $[\Gamma]_{\boldsymbol{R},\boldsymbol{R}'} = (-1)^{R_1+R_2}\delta_{\boldsymbol{R},\boldsymbol{R}'}$ [50].

We show that the semipositivity of Υ we addressed in the previous section leads to an important consequence. To be specific, as Υ is positive semidefinite, the smallest eigenvalue of $\tilde{\mathcal{H}}^{\text{sq}}$, $\varepsilon_{\text{min}}^{\text{sq}}$, satisfies $\varepsilon_{\text{min}}^{\text{sq}} \geqslant -4$. In addition, as $\tilde{\mathcal{H}}^{\text{sq}}$ is chiral symmetric, its largest eigenvalue $\varepsilon_{\text{max}}^{\text{sq}}$ is $-\varepsilon_{\text{min}}^{\text{sq}}$, so it satisfies $\varepsilon_{\text{max}}^{\text{sq}} \geqslant 4$. As -4 and 4 are the minimum and maximum of the eigenvalues for the square-lattice tight-binding model without the phase factor, the above facts provide a proof that the expansion of the band width by the introduction of the phase factor is prohibited.

III. NUMERICAL RESULTS FOR THE CHECKERBOARD MODEL

In this section, we present our numerical results for the random-phase MO model on a checkerboard lattice of Eq. (3).
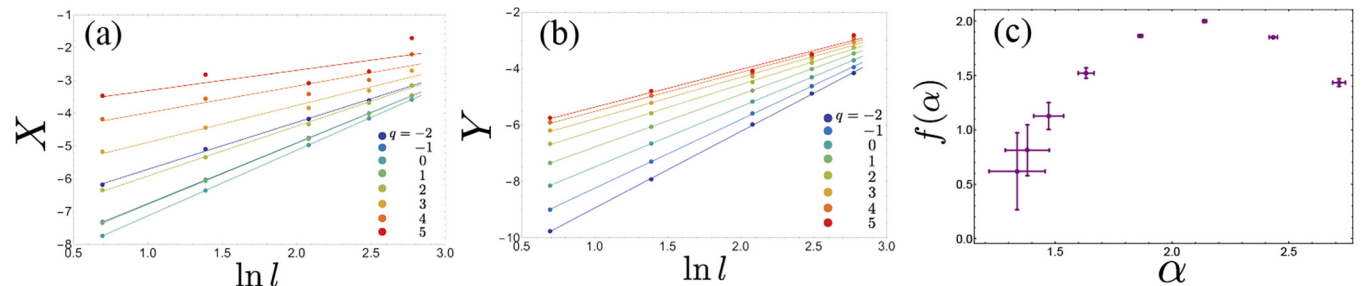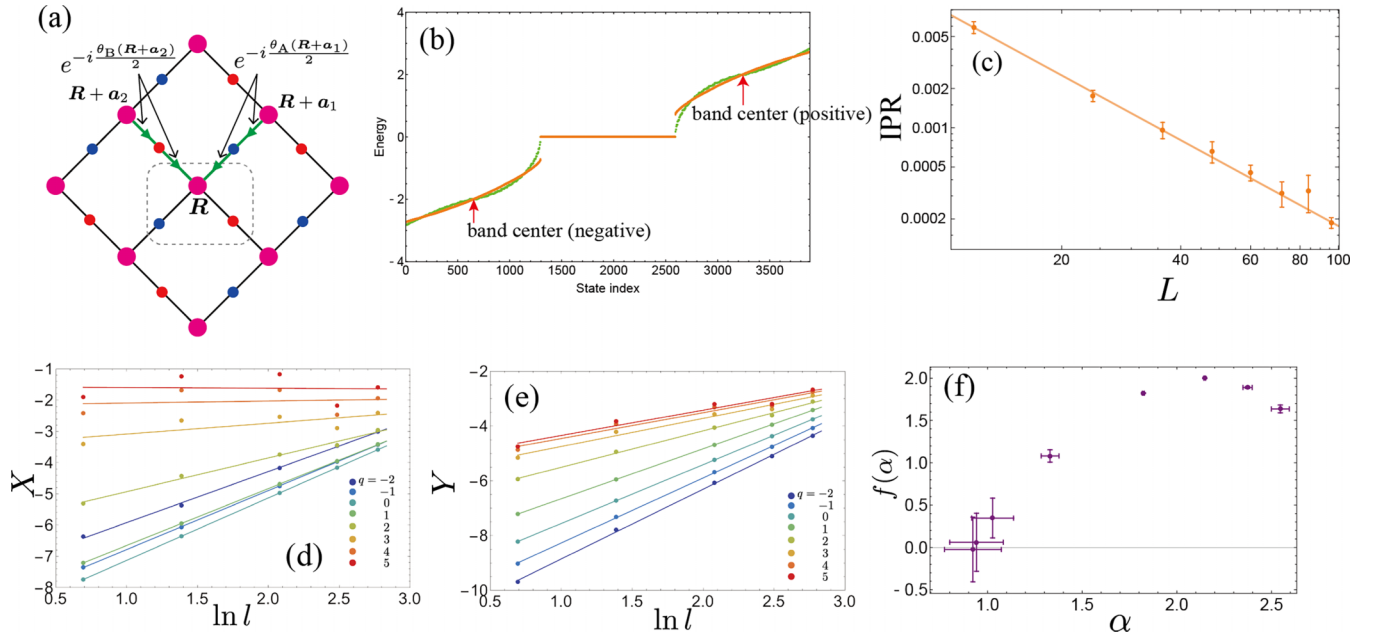

FIG. 6. Multifractal analysis for the center of the finite-energy modes. (a) X [Eq. (18)] and (b) Y [Eq. (19)] as functions of $\ln l$ for several values of q. (c) $f - \alpha$ spectrum. The error bars in panel (c) are the fitting errors for X and Y.

FIG. 7. (a) Schematic figure of the Lieb-lattice model of $\bar{\mathcal{H}}$. (b) The energy spectrum for the system with $L = 36$. Orange (green) dots correspond to the random (clean) system. (c) IPR for the center of the positive-energy sector. The average and standard deviations are calculated for ten samples of the configurations of θ's. The line represents the fitting function, IPR $= AL^{-B}$, with $A = 0.36$, $B = 1.65$. (d)–(f) Multifractal analysis for the center of the positive-energy sector. (d) X and (e) Y as functions of $\ln l$ for several values of q. (f) $f - \alpha$ spectrum. The error bars in panel (f) are the fitting errors for X and Y.

A. Energy spectrum

In Fig. 3(a), we show an energy spectrum in ascending order for $L = 36$. The orange dots correspond to the random-phase case, while the green dots correspond to the clean limit.
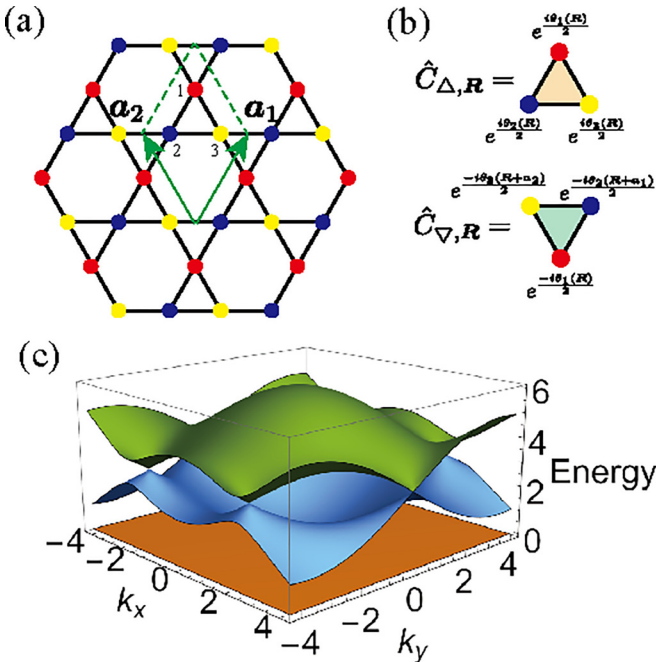
We clearly see degenerate zero-energy modes, whose degeneracy is $N_{\text{u.c.}} = L^2$. On top of the zero-energy modes, there exists a finite-energy gap, which is in sharp contrast to the clean limit, and to the real-valued random MO model [27,29]. In Fig. 3(b), we show the gap as a function of L, which indicates that the energy gap does not vanish when extrapolated to $L \to \infty$. The gap size is about 0.5. Recalling the relation between Υ and $\mathcal{H}$ and the relation of Eq. (10), we find that the gap Δ corresponds to the "shrinking" of the band width due to the random phase in the square-lattice tight-binding model. This shrinking of the band width was observed in the numerical simulations in the literature [32,34,35,40].

As we have seen in Sec. II A, the gap remains closed in the clean limit, so one may wonder how the gap evolves upon increasing the strength of disorders. To see this, we interpolate the disordered limit and the clean limit, To be specific, we modify the range of θ as $\theta_{\text{A/B}}(\boldsymbol{R}) \in [-\beta\pi, \beta\pi]$ with $\beta \in [0, 1]$. Figure 3(c) represents the β dependence of Δ for $L = 60$. We see that Δ is smoothly dependent on β, and it saturates around $\beta \sim 0.6$.

B. Wave functions: Emergent critical state at band center

Next, we reveal the characteristics of the wave functions for both degenerate zero modes and the finite-energy modes. Figure 4 shows the probability density, ρ. The definition of the probability density is as follows. For the finite-energy mode, it is defined as

$$\rho_\ell^{\text{NZM}}(i) = \left| \left[\boldsymbol{\phi}_\ell^{\text{NZM}} \right]_i \right|^2, \qquad (12)$$

where $\boldsymbol{\phi}_\ell^{\text{NZM}}$ $(\ell = 1, \ldots, N_{\text{u.c.}})$ is the ℓth nonzero energy eigenvector of $\mathcal{H}$ [see Eq. (9)]; here we align them such that

FIG. 8. (a) Kagome lattice. Two lattice vectors are $\boldsymbol{a}_1 = (\frac{1}{2}, \frac{\sqrt{3}}{2})$ and $\boldsymbol{a}_2 = (-\frac{1}{2}, \frac{\sqrt{3}}{2})$. (b) Schematic figure of $\hat{C}_{\triangle,\boldsymbol{R}}$ and $\hat{C}_{\triangledown,\boldsymbol{R}}$. (c) The dispersion relation for the clean limit [i.e., $\theta_{1/2/3}(\boldsymbol{R}) = 0$].
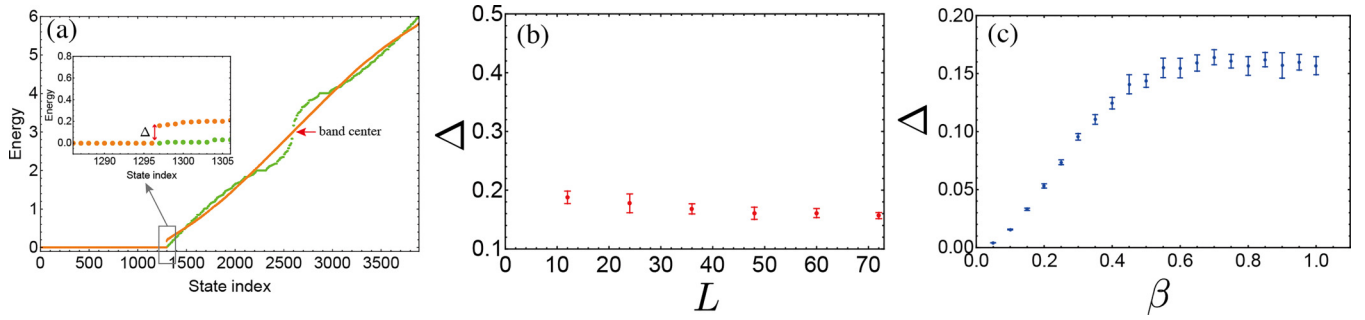
FIG. 9. (a) Energy spectrum for the system of the kagome lattice model with $L = 36$. Orange (green) dots correspond to the random (clean) system. (b) The gap Δ as a function of L. (c) The gap as a function of β for $L = 60$. The average and the standard deviation are calculated for ten independent configurations of θ's.

they satisfy $\varepsilon_1 \leqslant \varepsilon_2 \leqslant \cdots \leqslant \varepsilon_{N_{\text{u.c.}}}$. For the degenerate zero-energy modes, ρ is defined as

$$\rho^{\text{ZM}}(i) = \frac{1}{N_{\text{u.c.}}} \sum_{\ell=1}^{N_{\text{u.c.}}} \left| [\boldsymbol{\phi}_\ell^{\text{ZM}}]_i \right|^2. \qquad (13)$$

Note that the probability density satisfies $\sum_i \rho_\ell^{\text{NZM}}(i) = \sum_i \rho^{\text{ZM}}(i) = 1$, since the wave functions are normalized. We also note that $\rho_\ell^{\text{NZM}}(i)$ is related to the correlation matrix defined for $\boldsymbol{u}_\ell$ (see Appendix B for details).

Figures 4(a), 4(b), and 4(c) represent ρ for the zero modes, the nonzero mode of $\ell = 1$ (which we call the band edge), and the nonzero mode of $\ell = \frac{N_{\text{u.c.}}}{2}$ (which we call the band center), respectively. For the zero modes, we see that the distribution is rather uniform despite the existence of the randomness. At the band edge ($\ell = 1$), we see a sharp peak of the probability density, indicating the localized nature of the wave function. Interestingly, at the band center ($\ell = \frac{N_{\text{u.c.}}}{2}$), we see a spiky distribution of the probability density, indicating the critical nature of the wave function. In fact, the possibility of the critical state at the band center is inferred from Eq. (9). To be more specific, $\boldsymbol{u}_{N_{\text{u.c.}}/2}$, which is the wave function of the band center of $\tilde{\mathcal{H}}^{\text{sq}}$, is predicted to be critical [31–40]. Therefore, a naive expectation is that $\boldsymbol{\phi}_{N_{\text{u.c.}}/2}^{\text{NZM}}$ exhibits the same scaling behavior as $\boldsymbol{u}_{N_{\text{u.c.}}/2}$.

In order to examine the scaling behavior of the wave functions in more detail, we compute the system size dependence of the IPR. For the nonzero modes, we define the IPR as

$$\text{IPR}_\ell^{\text{NZM}} = \sum_i \left[\rho_\ell^{\text{NZM}}(i) \right]^2, \qquad (14)$$

and for the degenerate zero modes, we define it as

$$\text{IPR}^{\text{ZM}} = \sum_i \left[\rho^{\text{ZM}}(i) \right]^2. \qquad (15)$$

The results are shown in Fig. 5. Note that we focus on the zero-energy modes and the band center, as it is rather clear from Fig. 4(b) that the band edge is a localized state. We see that the IPR for the zero-energy modes is approximately fitted as $\text{IPR}^{\text{ZM}} \propto L^{-2}$, which is the scaling of the extended state. In fact, this is the same behavior as the zero modes of the real-valued random MO model [27,29], and thus is speculated to be ubiquitous in the zero modes of the random MO models. In contrast, for the band center, we see that the IPR is fitted as $\text{IPR}_{\ell=N_{\text{u.c.}}/2}^{\text{NZM}} \propto L^{-1.76}$, which is an intermediate behavior

between the localized and the extended states. Hence, this result supports that the band center is a critical state.

To further shed light on the critical nature of the band center, we perform the multifractal analysis. Specifically, we depict the $f-\alpha$ spectrum, by which we capture the multifractal nature of the wave function [51].

Let us briefly summarize how to obtain the $f-\alpha$ spectrum, which is based on Refs. [52,53]. First, we cover the system by the patches containing $l \times l$ unit cells. We label each patch by m. We then define the probability density in the patch m as

$$P(l; m) = \sum_{i \in m} \rho^{\text{NZM}}(i). \qquad (16)$$

Note that we omit the mode index ℓ for simplicity of writing. Then, using this, we define

$$\mu_m(q, l) = \frac{[P(l; m)]^q}{\sum_{m'} [P(l; m')]^q}. \qquad (17)$$

The key relations to extract the $f-\alpha$ spectrum from $\mu_m(q, l)$ are as follows:

$$X(q, l) := \sum_m \mu_m(q, l) \ln \mu_m(q, l) = f(q) \ln l \qquad (18)$$

and

$$Y(q, l) := \sum_m \mu_m(q, l) \ln \ln P_m(q, l) = \alpha(q) \ln l. \qquad (19)$$

Using (18) and (19), we find that the $f-\alpha$ spectrum can be obtained by (i) plotting $X(q, l)$ and $Y(q, l)$ as functions of $\ln l$ for several values of q and (ii) estimating $f(q)$ and $\alpha(q)$ from the slope of the plots of (i).

In Figs. 6(a) and 6(b), we plot X and Y as functions of $\ln l$, respectively. We set $L = 96$, $l = 2, 4, 8, 12, 16$, and $q = -2, -1, 0, 1, 2, 3, 4, 5$. We see that the fitting by using Eqs. (18) and (19) works well for $q \leqslant 3$, whereas the deviations of linear fitting for X become relatively large for $q = 4, 5$. On the basis of this fitting, we obtain the $f-\alpha$ spectrum, as shown in Fig. 6(c). We clearly see the characteristic downward convex behavior of the $f-\alpha$ spectrum. This indicates the multifractal nature of the wave function, which is characteristic to the critical state.

Combining the results of the IPR and that of the multifractal analysis, we conclude that the checkerboard model $\mathcal{H}$ hosts the critical state at the center of the finite-energy sector. Before proceeding further, we remark on a role of symmetry.

In the square-lattice random-phase model, it has been argued that the chiral symmetry represented by Γ (see Sec. II C) plays an essential role in realizing the critical state. Meanwhile the Hamiltonian $\mathcal{H}$ itself does not preserve the chiral symmetry, although the critical state appearing in this model is inherited from the chiral symmetric model, $\mathcal{H}^{\mathrm{sq}}$. In other words, $\mathcal{H}$ serves as an example of the random tight-binding model in unitary class realizing the critical state without preserving chiral symmetry.

IV. THE COMPOSITE MODEL CONSTRUCTED FROM MOLECULAR ORBITALS: A LIEB-LATTICE MODEL

So far, we have investigated the checkerboard model constructed by the MOs with random U(1) variable whose Hamiltonian matrix is given as $\mathcal{H}$. There, the existence of the critical state at the center of the finite-energy states is inherited from that of the square-lattice random-phase model. In this section, we point out that the same trick to obtain the critical state is applicable to the composite of the square and the checkerboard lattices, that is, the Lieb lattice. In fact, we have already introduced the Lieb-lattice model, $\bar{\mathcal{H}}$, in Eq. (5) to account for the semipositivity of $\mathcal{H}$. The schematic figure of the Lieb-lattice model is shown in Fig. 7(a).

We first remark that the matrix $\bar{\mathcal{H}}$ is chiral symmetric, namely, $\bar{\mathcal{H}}$ satisfies $\{\bar{\mathcal{H}}, \bar{\Gamma}\} = 0$ with

$$\bar{\Gamma} = \begin{pmatrix} \hat{I}_{N_{\mathrm{u.c.}}} & \mathcal{O}_{N_{\mathrm{u.c.}}, 2N_{\mathrm{u.c.}}} \\ \mathcal{O}_{2N_{\mathrm{u.c.}}, N_{\mathrm{u.c.}}} & -\hat{I}_{2N_{\mathrm{u.c.}}} \end{pmatrix}. \quad (20)$$

From Eq. (20), we find $|\mathrm{Tr}(\bar{\Gamma})| = N_{\mathrm{u.c.}}$. Due to this relation, there exist $N_{\mathrm{u.c.}}$ zero modes [54–57]. Also, the chiral symmetry itself implies that the finite-energy states appear at positive and negative in a pairwise manner. Such behaviors are indeed seen in Fig. 7(b), where we plot the energy spectrum of the Lieb-lattice model for $L = 36$.

Let us now argue the characters of the wave functions. Importantly, the finite-energy eigenvectors of $\bar{\mathcal{H}}$ are also constructed from the eigenvectors of Υ, $\boldsymbol{u}_\ell$. More precisely, the vector $\boldsymbol{\varphi}_\ell^+ = \frac{1}{\mathcal{N}_\ell}(\sqrt{\varepsilon_\ell}\boldsymbol{u}_\ell, \Psi\boldsymbol{u}_\ell)^{\mathrm{T}}$ is the normalized eigenvector of $\bar{\mathcal{H}}$ with the eigenvector $\sqrt{\varepsilon_\ell}$, where $\mathcal{N}_\ell$ is the normalization constant; in fact, noting that $|\boldsymbol{u}_\ell|^2 = 1$ and $|\Psi\boldsymbol{u}_\ell|^2 = \varepsilon_\ell$, one finds $\mathcal{N}_\ell = \sqrt{2\varepsilon_\ell}$. One can easily check this by explicitly multiplying $\bar{\mathcal{H}}$ to $\boldsymbol{\varphi}_\ell^+$:

$$\bar{\mathcal{H}}\boldsymbol{\varphi}_\ell^+ = \frac{1}{\mathcal{N}_\ell}\begin{pmatrix} \Psi^\dagger\Psi\boldsymbol{u}_\ell \\ \sqrt{\varepsilon_\ell}\Psi\boldsymbol{u}_\ell \end{pmatrix} = \frac{\sqrt{\varepsilon_\ell}}{\mathcal{N}_\ell}\begin{pmatrix} \sqrt{\varepsilon_\ell}\boldsymbol{u}_\ell \\ \Psi\boldsymbol{u}_\ell \end{pmatrix} = \sqrt{\varepsilon_\ell}\boldsymbol{\varphi}_\ell^+. \quad (21)$$

Its negative-energy counterpart, i.e., the one whose eigenenergy is $-\sqrt{\varepsilon_\ell}$, is given as $\boldsymbol{\varphi}_\ell^- = \bar{\Gamma}\boldsymbol{\varphi}_\ell^- = \frac{1}{\mathcal{N}_\ell}(\sqrt{\varepsilon_\ell}\boldsymbol{u}_\ell, -\Psi\boldsymbol{u}_\ell)^{\mathrm{T}}$. Obviously, $\boldsymbol{\varphi}_\ell^-$ has the same probability density distribution as that of $\boldsymbol{\varphi}_\ell^+$.

Then, considering the fact that $\boldsymbol{u}_\ell$ and $\Psi\boldsymbol{u}_\ell$ are the critical states for ℓ being the band center, we expect that the corresponding $\boldsymbol{\varphi}_\ell^{+/-}$ are critical as well. We examine the above conjecture by the numerical calculation. In Fig. 7(c), we plot the IPR for $\boldsymbol{\varphi}_\ell^+$ for ℓ being the band center as a function of L. It exhibits the system size dependence, IPR $\propto L^{-1.65}$, which indicates that the wave function is neither localized nor extended. Further, in Figs. 7(d)–7(f), we show the results of the multifractal analysis. We see that the deviation from the

linear fitting for X for $q = 4, 5$ becomes larger than that for the checkerboard model. In fact, for these values of q, X becomes almost independent of the patch size ℓ. Nevertheless, the characteristic downward convex behavior of the $f - \alpha$ curve is still observed, which indicates the multifractal nature of the wave function. From these results, we conclude that the Lieb-lattice model $\bar{\mathcal{H}}$ also hosts the critical state. Additionally, as the probability density of $\boldsymbol{\varphi}_\ell^-$ is the same as the corresponding $\boldsymbol{\varphi}_\ell^+$, the critical state also exists in the negative-energy sector. It is noteworthy that the chiral symmetry of $\bar{\mathcal{H}}$ is not a direct origin of the emergence of the critical states, because the critical states have finite energy rather than zero energy.

V. KAGOME LATTICE MODEL AND DECORATED HONEYCOMB LATTICE MODEL

In this section, we show that the same construction of the random-phase MO model, discussed in Sec. II, can be applied to the kagome lattice [Fig. 8(a)].

We consider the tight-binding model:

$$H = \sum_{\boldsymbol{R}} \hat{C}_{\triangle,\boldsymbol{R}}^\dagger \hat{C}_{\triangle,\boldsymbol{R}} + \hat{C}_{\triangledown,\boldsymbol{R}}^\dagger \hat{C}_{\triangledown,\boldsymbol{R}}, \quad (22)$$

where

$$\hat{C}_{\triangle,\boldsymbol{R}} = e^{i\theta_1(\boldsymbol{R})/2}c_{\boldsymbol{R},1} + e^{i\theta_2(\boldsymbol{R})/2}c_{\boldsymbol{R},2} + e^{i\theta_3(\boldsymbol{R})/2}c_{\boldsymbol{R},3} \quad (23)$$

and

$$\hat{C}_{\triangledown,\boldsymbol{R}} = e^{-i\theta_1(\boldsymbol{R})/2}c_{\boldsymbol{R},1} + e^{-i\theta_2(\boldsymbol{R}+\boldsymbol{a}_1)/2}c_{\boldsymbol{R},2} + e^{-i\theta_3(\boldsymbol{R}+\boldsymbol{a}_2)/2}c_{\boldsymbol{R},3}. \quad (24)$$

The phase factors $\theta_{1,2,3}(\boldsymbol{R}) \in [-\pi, \pi]$ again obey the uniform distribution. See Fig. 8(b) for the schematics of $\hat{C}_{\triangle/\triangledown,\boldsymbol{R}}$. Note that the dual counterpart of this model, Υ, corresponds to the random-phase model on a honeycomb lattice with uniform on-site potential being 3. In the clean limit, we have three bands; the flat band has the lowest energy, and the remaining two bands form Dirac cones at the K and K' points [Fig. 8(c)].

In the following, we show the numerical data for this model. As we will see, all results are qualitatively the same as that for the checkerboard model.

Figure 9(a) shows the energy spectrum for $L = 36$. We again see macroscopically degenerate zero modes even in the presence of the randomness. Similarly to the checkerboard model, we see a finite gap between the zero modes and the bottom of the finite-energy modes. As for the size dependence of the gap [Fig. 9(b)], we again see that the gap is expected to be nonvanishing for $L \to \infty$. The gap size is about 0.15, which is smaller than that for the checkerboard model. Additionally, the β dependence of the gap [Fig. 9(c)] shows similar behavior as that for the checkerboard model.

We next analyze the probability density distribution in the real space. Figures 10(a), 10(b), and 10(c) show the probability density distributions for the zero modes, the band edge, and the band center, respectively. We again see qualitatively similar behaviors to the checkerboard model. In particular, the probability density for the band center seems to have a spiky distribution, which implies the multifractal nature.

Figures 11(a) and 11(b) show the system size dependence of the IPR for the zero modes and the band center,
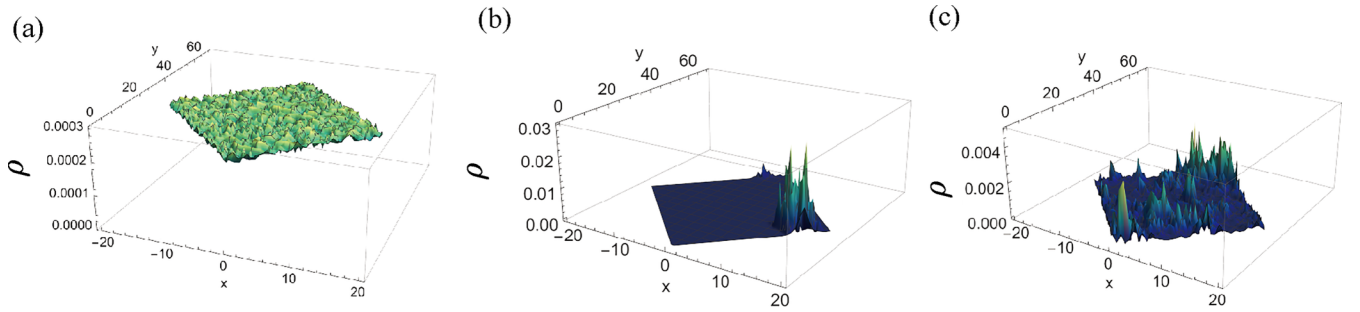
FIG. 10. The probability density for (a) the zero modes, (b) the lowest finite-energy mode, and (c) the center of the finite-energy modes for the kagome lattice model. We set $L = 36$.

respectively. We see that the IRP has a scaling behavior of the extended state for the zero modes, whereas that for the band center is of neither the extended state nor the localized state (IPR $\propto L^{-1.78}$).

Figure 12 shows the results of the multifractal analysis for a band center. We again see that X and Y are linear in $\ln l$, and that the $f - \alpha$ curve is downward convex, indicating the multifractal nature.

Finally, we introduce a model corresponding to $\bar{\mathcal{H}}$, i.e., the composite of the honeycomb and kagome lattices. That model is called the decorated honeycomb lattice model, whose schematic figure is shown in Fig. 13(a). In the energy spectrum [Fig. 13(b)], we see degenerate zero modes and

the finite-energy modes appearing in a pairwise manner in positive- and negative-energy sectors.

Further, as is the case in the Lieb lattice, the band center of the finite-energy modes is again expected to be critical. This is numerically indicated by the scaling behavior of the IPR [Fig. 13(c)]. As for the results of the multifractal analysis [Figs. 13(d)–13(f)], we see the same tendency as those of the Lieb lattice [Figs. 7(d)–7(f)]. Specifically, the results for $q = 4, 5$ contain large fitting errors, but we believe it reasonable to judge that the downward convex of the $f - \alpha$ spectrum is observed from the data of $q = -2, \ldots, 3$.

VI. SUMMARY

We have proposed a class of tight-binding models constructed by the representation with random U(1) variables. The model construction scheme guarantees the existence of the macroscopically degenerate zero modes. A key insight is that the models constructed in this way have their dual counterparts, which are the random-phase hopping models on bipartite lattices. As such, various important properties of eigenvalues and wave functions are closely tied with a dual counterpart.

By the numerical calculations, we show a gap opening on top of the zero-energy modes, which is in contrast to the real-value random MO model. The probability density distribution of the zero-energy modes has a scaling property of the extended state, similar to that of the real-value random MO model. Besides the zero modes, we also find that the band center of the finite-energy sector is the critical state, as demonstrated by the scaling of IPR and the characteristic $f - \alpha$ spectrum. Importantly, the critical state is inherited from its dual counterpart, which is chiral symmetric, but the random-phase MO models themselves are lattice models hosting the critical state without preserving the chiral symmetry.

Furthermore, as a by-product of this model-construction scheme, we introduce yet another random U(1)-valued hopping model defined on a composite lattice such as Lieb and decorated honeycomb lattices, which host the critical states appearing in a pairwise manner in positive- and negative-energy sectors.

Before closing this paper, we address several future problems which we believe deserve being studied. Firstly, the models we have studied are two-dimensional models, but the random U(1) MO models in higher dimensions can be constructed straightforwardly. Such higher-dimensional
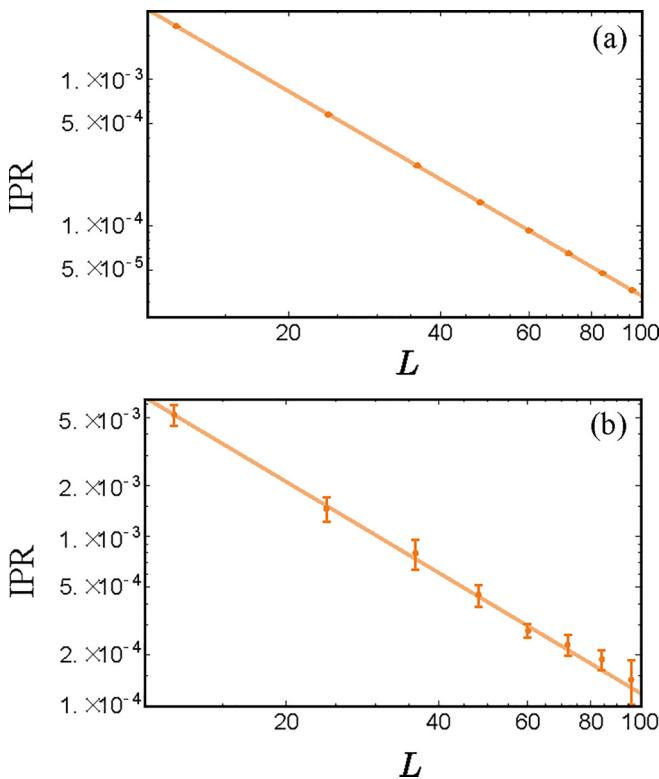

FIG. 11. IPR for (a) the degenerate zero modes and (b) the center of the finite-energy modes of the kagome lattice model. The average and standard deviation is calculated for ten samples of the configurations of θ's. The line represents the fitting function, IPR $= AL^{-B}$, with (a) $A = 0.33$, $B = 2.00$ and (b) $A = 0.43$, $B = 1.78$.
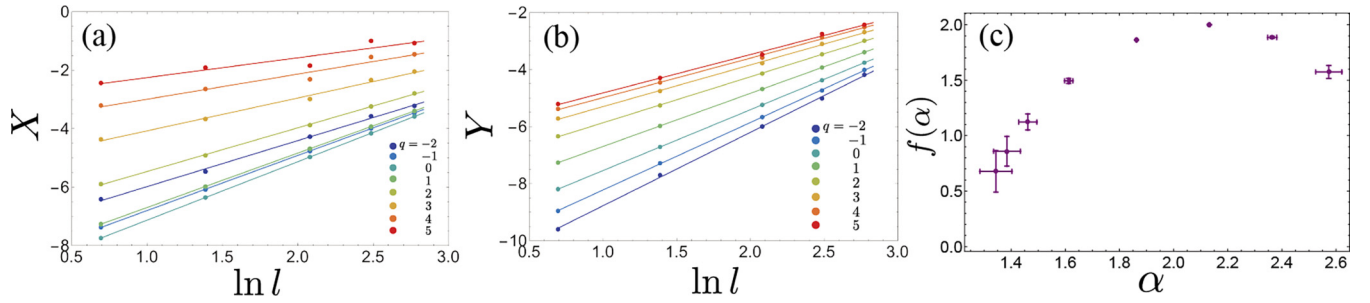
FIG. 12. Multifractal analysis for the center of the finite-energy modes of the kagome lattice model. (a) X and (b) Y as functions of $\ln l$ for several values of q. (c) $f-\alpha$ spectrum. The error bars in the panel (c) are the fitting errors for X and Y.

models will be a promising target for investigating characteristic localization phenomena, as is the case of the conventional random-phase model [58,59]. Secondly, the MO representation is applicable to other symmetry classes. For instance, if we adopt random SU(2) matrices as coefficients of MOs, we obtain random flat-band models in the symplectic class. Studying localization phenomena in such models, for both degenerate zero modes and finite-energy modes, will be an intriguing future problem. Finally, experimental realization of the random U(1) MO models and the corresponding composite-lattice models is an important issue. In fact, the models considered in this paper contain only the on-site potentials and the nearest-neighbor hoppings, which makes these models feasible in some artificial systems. In cold atoms [60], photonic waveguides [61], and electric circuits [62], the complex hoppings can be implemented, so we expect that appropriate control of their amplitudes and phases will pro-

vide chances of realizing our models. For instance, in electric circuits, systematic control of the admittance of the circuit element can be achieved by using the variable resistors and capacitors [63], which will open the way to realize the desired random complex hoppings.

APPENDIX A: REMARK ON EQ. (2)

At first glance, the choice of MOs in Eq. (2) is fine-tuned, since the phase factors appearing in neighboring MOs are not independent. An alternative and more naive way of
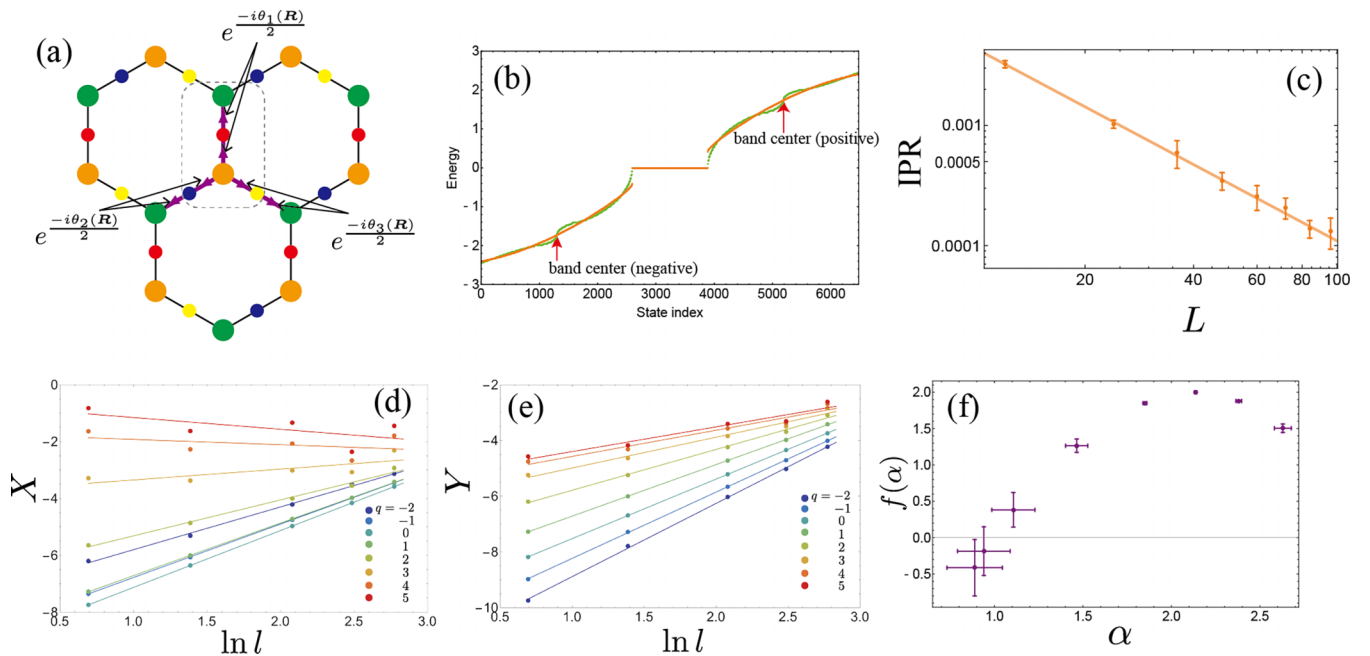

FIG. 13. (a) Schematic figure of the decorated honeycomb lattice model. (b) The energy spectrum for the system with $L = 36$. Orange (green) dots correspond to the random (clean) system. (c) IPR for the center of the positive-energy sector. The average and standard deviation is calculated for ten samples of the configurations of θ's. The line represents the fitting function, IPR $= AL^{-B}$, with $A = 0.17$, $B = 1.60$. (d)–(f) Multifractal analysis for the center of the positive-energy sector. (d) X and (e) Y as functions of $\ln l$ for several values of q. (f) $f-\alpha$ spectrum. The error bars in panel (f) are the fitting errors for X and Y.

introducing the phase is

$$
\hat{\tilde{C}}_{\boldsymbol{R}} = e^{i\tilde{\theta}_1(\boldsymbol{R})} c_{\boldsymbol{R},\mathrm{A}} + e^{i\tilde{\theta}_2(\boldsymbol{R})} c_{\boldsymbol{R},\mathrm{B}}
$$
$$
+ e^{i\tilde{\theta}_3(\boldsymbol{R})} c_{\boldsymbol{R}+\boldsymbol{a}_1,\mathrm{A}} + e^{i\tilde{\theta}_4(\boldsymbol{R})} c_{\boldsymbol{R}+\boldsymbol{a}_2,\mathrm{B}}, \quad \text{(A1)}
$$

where $\tilde{\theta}_{1,2,3,4}(\boldsymbol{R})$ are random variables. Note that the numbers of θ variables are $2N_{\mathrm{u.c.}}$ for (2) and $4N_{\mathrm{u.c.}}$ for (A1). Here we show that (2) and (A1) give the same Hamiltonian under the gauge transformation. Specifically, defining $d_{\boldsymbol{R},\mathrm{A}} := e^{i[\tilde{\theta}_1(\boldsymbol{R})+\tilde{\theta}_3(\boldsymbol{R}-\boldsymbol{a}_1)]/2} c_{\boldsymbol{R},\mathrm{A}}$ and $d_{\boldsymbol{R},\mathrm{B}} := e^{i[\tilde{\theta}_2(\boldsymbol{R})+\tilde{\theta}_4(\boldsymbol{R}-\boldsymbol{a}_2)]/2} c_{\boldsymbol{R},\mathrm{B}}$, we have

$$
\hat{\tilde{C}}_{\boldsymbol{R}} = e^{i[\tilde{\theta}_1(\boldsymbol{R})-\tilde{\theta}_3(\boldsymbol{R}-\boldsymbol{a}_1)]/2} d_{\boldsymbol{R},\mathrm{A}} + e^{i[\tilde{\theta}_2(\boldsymbol{R})-\tilde{\theta}_4(\boldsymbol{R}-\boldsymbol{a}_2)]/2} d_{\boldsymbol{R},\mathrm{B}}
$$
$$
+ e^{-i[\tilde{\theta}_1(\boldsymbol{R}+\boldsymbol{a}_1)-\tilde{\theta}_3(\boldsymbol{R})]/2} d_{\boldsymbol{R}+\boldsymbol{a}_1,\mathrm{A}}
$$
$$
+ e^{-i[\tilde{\theta}_2(\boldsymbol{R}+\boldsymbol{a}_2)-\tilde{\theta}_4(\boldsymbol{R})]/2} d_{\boldsymbol{R}+\boldsymbol{a}_2,\mathrm{B}}. \quad \text{(A2)}
$$

Then, by setting $\tilde{\theta}_1(\boldsymbol{R}) - \tilde{\theta}_3(\boldsymbol{R} - \boldsymbol{a}_1) = \theta_{\mathrm{A}}(\boldsymbol{R})$ and $\tilde{\theta}_2(\boldsymbol{R}) - \tilde{\theta}_4(\boldsymbol{R} - \boldsymbol{a}_2) = \theta_{\mathrm{B}}(\boldsymbol{R})$, we find that $\hat{\tilde{C}}_{\boldsymbol{R}}$ of Eq. (A2) is equivalent to $\hat{C}_{\boldsymbol{R}}$ of Eq. (2).

APPENDIX B: PROBABILITY DENSITY OF FINITE-ENERGY MODES

In this Appendix, we show that the probability density of the finite-energy mode in Eq. (12) can be written by using Ψ and the correlation matrix defined for $\boldsymbol{u}_\ell$. This is archived by simply substituting Eq. (9) into Eq. (12):

$$
\rho_\ell^{\mathrm{NZM}}(i) = [\boldsymbol{\phi}_\ell^{\mathrm{NZM}}]_i [(\boldsymbol{\phi}_\ell^{\mathrm{NZM}})^\dagger]_i
$$
$$
= \frac{1}{\varepsilon_\ell} [\Psi \boldsymbol{u}_\ell]_i [(\boldsymbol{u}_\ell)^\dagger \Psi^\dagger]_i
$$
$$
= \frac{1}{\varepsilon_\ell} [\Psi g^\ell \Psi^\dagger]_{ii}. \quad \text{(B1)}
$$

Here, g^ℓ is the $N_{\mathrm{u.c.}} \times N_{\mathrm{u.c.}}$ matrix,

$$
[g^\ell]_{\boldsymbol{R},\boldsymbol{R}'} = [\boldsymbol{u}_\ell]_{\boldsymbol{R}} [\boldsymbol{u}_\ell^*]_{\boldsymbol{R}'}, \quad \text{(B2)}
$$

which is referred to as the correlation matrix.

[1] P. W. Anderson, Phys. Rev. **109**, 1492 (1958).
[2] E. Abrahams, P. W. Anderson, D. C. Licciardello, and T. V. Ramakrishnan, Phys. Rev. Lett. **42**, 673 (1979).
[3] Y. Hatsugai and P. A. Lee, Phys. Rev. B **48**, 4204 (1993).
[4] C. de C. Chamon, C. Mudry, and X.-G. Wen, Phys. Rev. B **53**, R7638 (1996).
[5] Y. Hatsugai, X.-G. Wen, and M. Kohmoto, Phys. Rev. B **56**, 1061 (1997).
[6] H. E. Castillo, C. de C. Chamon, E. Fradkin, P. M. Goldbart, and C. Mudry, Phys. Rev. B **56**, 10668 (1997).
[7] Y. Morita and Y. Hatsugai, Phys. Rev. Lett. **79**, 3728 (1997).
[8] T. Fukui, Phys. Rev. B **68**, 153307 (2003).
[9] M. E. Zhitomirsky and H. Tsunetsugu, Phys. Rev. B **70**, 100403(R) (2004).
[10] D. L. Bergman, C. Wu, and L. Balents, Phys. Rev. B **78**, 125104 (2008).
[11] Y. Kuno, T. Mizoguchi, and Y. Hatsugai, Phys. Rev. B **102**, 241115(R) (2020).
[12] M. Goda, S. Nishino, and H. Matsuda, Phys. Rev. Lett. **96**, 126401 (2006).
[13] S. Nishino, H. Matsuda, and M. Goda, J. Phys. Soc. Jpn. **76**, 024709 (2007).
[14] J. T. Chalker, T. S. Pickles, and P. Shukla, Phys. Rev. B **82**, 104209 (2010).
[15] D. Leykam, S. Flach, O. Bahat-Treidel, and A. S. Desyatnikov, Phys. Rev. B **88**, 224203 (2013).
[16] P. Shukla, Phys. Rev. B **98**, 054206 (2018).
[17] P. Shukla, Phys. Rev. B **98**, 184202 (2018).
[18] T. Bilitewski and R. Moessner, Phys. Rev. B **98**, 235109 (2018).
[19] Y. Kuno, T. Mizoguchi, and Y. Hatsugai, Phys. Rev. B **104**, 085130 (2021).
[20] A. Altland and M. R. Zirnbauer, Phys. Rev. B **55**, 1142 (1997).
[21] For simplicity, we assume that there is one AO at each lattice site. Extension to spinful and/or multiorbital cases will be an intriguing future problem.
[22] Y. Hatsugai and I. Maruyama, Europhys. Lett. **95**, 20003 (2011).
[23] Y. Hatsugai, K. Shiraishi, and H. Aoki, New J. Phys. **17**, 025009 (2015).
[24] T. Mizoguchi and Y. Hatsugai, Europhys. Lett. **127**, 47001 (2019).
[25] T. Mizoguchi and Y. Hatsugai, Phys. Rev. B **101**, 235125 (2020).
[26] T. Mizoguchi, Y. Kuno, and Y. Hatsugai, Phys. Rev. B **104**, 035161 (2021).
[27] Y. Hatsugai, Ann. Phys. **435**, 168453 (2021).
[28] T. Mizoguchi, Y. Kuno, and Y. Hatsugai, Prog. Theor. Exp. Phys. **2022**, 023I02 (2022).
[29] T. Kuroda, T. Mizoguchi, H. Araki, and Y. Hatsugai, J. Phys. Soc. Jpn. **91**, 044703 (2022).
[30] More precisely, in the models we have studied so far, the amplitudes of the real-valued coefficients are random.
[31] P. A. Lee and D. S. Fisher, Phys. Rev. Lett. **47**, 882 (1981).
[32] C. Pryor and A. Zee, Phys. Rev. B **46**, 3116 (1992).
[33] V. Kalmeyer, D. Wei, D. P. Arovas, and S. Zhang, Phys. Rev. B **48**, 11095 (1993).
[34] T. Sugiyama and N. Nagaosa, Phys. Rev. Lett. **70**, 1980 (1993).
[35] T. Ohtsuki, K. Slevin, and Y. Ono, J. Phys. Soc. Jpn. **62**, 3979 (1993).
[36] Y. Avishai, Y. Hatsugai, and M. Kohmoto, Phys. Rev. B **47**, 9561 (1993).
[37] R. Gade, Nucl. Phys. B **398**, 499 (1993).
[38] A. W. W. Ludwig, M. P. A. Fisher, R. Shankar, and G. Grinstein, Phys. Rev. B **50**, 7526 (1994).
[39] J. Miller and J. Wang, Phys. Rev. Lett. **76**, 1461 (1996).
[40] A. Furusaki, Phys. Rev. Lett. **82**, 604 (1999).
[41] T. Mizoguchi, Y. Kuno, and Y. Hatsugai, Phys. Rev. A **102**, 033527 (2020); **104**, 029906(E) (2021).
[42] T. Mizoguchi, T. Yoshida, and Y. Hatsugai, Phys. Rev. B **103**, 045136 (2021).
[43] J.-W. Rhim and B.-J. Yang, Phys. Rev. B **99**, 045107 (2019).
[44] Y. Hwang, J.-W. Rhim, and B.-J. Yang, Phys. Rev. B **104**, L081104 (2021).

[45] Y. Hwang, J.-W. Rhim, and B.-J. Yang, Phys. Rev. B **104**, 085144 (2021).

[46] A. Graf and F. Piéchon, Phys. Rev. B **104**, 195128 (2021).

[47] P. Di Francesco and J.-B. Zuber, Nucl. Phys. B **338**, 602 (1990).

[48] P. A. Pearce and Y.-K. Zhou, Int. J. Mod. Phys. B **07**, 3649 (1993).

[49] T. Mizoguchi, H. Katsura, I. Maruyama, and Y. Hatsugai, Phys. Rev. B **104**, 035155 (2021).

[50] Strictly speaking, under the periodic boundary condition, the chiral symmetry is preserved only when L is even.

[51] T. C. Halsey, M. H. Jensen, L. P. Kadanoff, I. Procaccia, and B. I. Shraiman, Phys. Rev. A **33**, 1141 (1986).

[52] A. Chhabra and R. V. Jensen, Phys. Rev. Lett. **62**, 1327 (1989).

[53] A. B. Chhabra, C. Meneveau, R. V. Jensen, and K. R. Sreenivasan, Phys. Rev. A **40**, 5284 (1989).

[54] E. H. Lieb, Phys. Rev. Lett. **62**, 1201 (1989).

[55] X. Wen and A. Zee, Nucl. Phys. B **316**, 641 (1989).

[56] P. W. Brouwer, E. Racine, A. Furusaki, Y. Hatsugai, Y. Morita, and C. Mudry, Phys. Rev. B **66**, 014204 (2002).

[57] M. Koshino, T. Morimoto, and M. Sato, Phys. Rev. B **90**, 115207 (2014).

[58] T. Ohtsuki, Y. Ono, and B. Kramer, J. Phys. Soc. Jpn. **63**, 685 (1994).

[59] T. Kawarabayashi, B. Kramer, and T. Ohtsuki, Phys. Rev. B **57**, 11842 (1998).

[60] J. Dalibard, F. Gerbier, G. Juzeliūnas, and P. Öhberg, Rev. Mod. Phys. **83**, 1523 (2011).

[61] S. Mukherjee, M. Di Liberto, P. Öhberg, R. R. Thomson, and N. Goldman, Phys. Rev. Lett. **121**, 075502 (2018).

[62] T. Hofmann, T. Helbig, C. H. Lee, M. Greiter, and R. Thomale, Phys. Rev. Lett. **122**, 247702 (2019).

[63] K. Yatsugi, T. Yoshida, T. Mizoguchi, Y. Kuno, H. Iizuka, Y. Tadokoro, and Y. Hatsugai, Commun. Phys. **5**, 180 (2022).